Article:
Xia, D, Xu, Y orcid.org/0000-0001-5180-8892, Mannering, J et al. (6 more authors) (2021) Tuning the Electrical and Solar Thermal Heating Efficiencies of Nanocarbon Aerogels. Chemistry of Materials, 33 (1). pp. 392-402. ISSN 0897-4756

https://doi.org/10.1021/acs.chemmater.0c04166

Tuning the Electrical and Solar-Thermal Heating Efficiencies of Nanocarbon Aerogels

Dong Xia,[1] Yifei Xu,[1] Jamie Mannering,[1] Xiaolong Ma,[2] M. S. Ismail,[3] Duncan Borman,[4] Daniel L. Baker,[5] Mohamed Pourkashanian[3] and Robert Menzel[1]*

[1] School of Chemistry, University of Leeds, Leeds, UK.

[2] School of Chemical and Process Engineering, University of Leeds, Leeds, UK.

[3] Department of Mechanical Engineering, The University of Sheffield, Sheffield, UK.

[4] School of Civil Engineering, University of Leeds, Leeds, UK.

[5] School of Physics and Astronomy, University of Leeds, LS2 9JT, Leeds, UK

* Corresponding authors: Dong Xia, Email: cmdx@leeds.ac.uk, Tel: +44(0)7596218478

Abstract: Nanocarbon aerogels display outstanding electrical and solar-thermal heating efficiencies. However, little is known about the relationship between their microstructure and the heating performance. In this study, two different types of carbon nanotube (CNT) aerogels were synthesized via an ice-templating (IT) and emulsion-templating (ET) approach, respectively, which induces drastic difference in internal microstructures, crosslinking densities and porosities. These structural differences give rise to substantial efficiency differences in electrical aerogel heating (e.g. 46 ^{o}C/W for rET-CNT aerogel, 75 ^{o}C/W for rIT-CNT aerogel). Systematic comparison of nanocarbon aerogel microstructure in terms of nanocarbon type, envelope density, and nanocarbon graphiticity shows that the Joule-heating efficiency is highly correlated with the thermal conductivities of the aerogels, where aerogels with lower thermal conductivities exhibit higher Joule-heating efficiencies. This relationship is also observed for solar-thermal aerogel heating, with the aerogels of lowest thermal conductivity (rIT-CNT aerogel) exhibiting a 30% higher efficiency in solar water evaporation, compared to rET-CNT aerogels. These results demonstrate that the heating properties of nanocarbon aerogels can be readily tuned and enhanced through structural control alone. The findings provide a new perspective for the design of nanocarbon aerogel for applications that involve electrical or solar-thermal heating, such as temperature-dependent separation, sorption, sensing, and catalysis.

Introduction

Nanocarbon aerogels have been widely explored as high-performance functional materials in sorption,[1] catalysis,[2] fuel purification,[3, 4] energy storage[5] and sensing.[6] Recently, nanocarbon-based aerogels have also shown great promise for desalination and solar steam evaporation applications,[7, 8] which are important for the development of new clean water technologies.

Importantly, nanocarbon aerogels also find increasingly use as stabilizing 3D support frameworks for different types of functional nanoparticles to form decorated hybrid nanocarbon aerogels. For example, Liu et al. synthesized hybrid graphene aerogels with uniform decoration of low-cost Fe_2O_3 nanoparticles, which exhibited remarkable lithium ion storage performance.[9] Another interesting example includes the fabrication of eco-friendly hybrid metal-organic-framework/CNT aerogels by Liang et al., which showed excellent capacities for the adsorptive removal of pesticides from water.[10] A highly interesting feature of nanocarbon aerogels, in the context of many of these applications, is their potential to be directly heated through the application of an electrical current (Joule-heating)[11, 12] or through solar irradiation (solar thermal energy conversion).[13, 14] This can be used, e.g. to activate desired chemical processes at elevated temperatures, to thermally regenerate materials after use, or to accelerate physical processes such as water evaporation. The 3D interconnected graphitic microstructure of the electrically-conducting aerogel framework enables uniform local electrical heating across the entire porous material, resulting in faster, more efficient and more homogeneous heating, compared to conventional external heating processes (e.g. in an oven or furnace).[11] For instance, it has been shown that a typical reduced graphene oxide (rGO) aerogel can be accurately and repeatedly Joule-heated to a desired temperature at relatively low electrical potentials, high heating efficiency (45 °C/W), very fast heating speeds (600 K/min), and low energy consumption.[11] This feature has already been used for some preliminary applications, e.g. direct resistive Joule-heating has been employed to thermally regenerate functional graphene and CNT aerogels at temperatures between 100-400 °C for highly sensitive gas sensing[6] and adsorptive fuel desulfurization.[3, 4] Meanwhile, Joule-heating was also successfully employed for precise temperature control of Ag/Co_3O_4/Carbon hybrid aerogel catalysts, used for efficient catalytic formaldehyde oxidation at 90 °C.[15] Direct electro-thermal heating of interconnected 3D

nanocarbon networks has also been exploited for polymer curing[16-18] and for the detection of structural damage in polymer nanocomposites through thermal IR imaging.[19] Joule-heating has also been proven as an energy efficient approach to induce heating in graphene-wrapped polymeric sponges in order to thermally enhance their performance as crude-oil clean-up agents.[20]

Nanocarbon aerogels have also been repeatedly studied as solar thermal conversion materials for solar water evaporation, an emerging technology important for water desalination, liquid-phase separation and sterilization applications.[21-23] In these studies, heat is generated through absorption of solar light.[24] The heat generated upon light absorption can be utilized to promote water evaporation (solar steam generation).[25] Such a method usually requires porous solar thermal conversion materials that could float on top of the water surface, so that heat generated from solar irradiation can directly contribute to water evaporation, overall reducing process duration and lowering energy costs. Nanocarbon aerogels are therefore ideal for solar water evaporation due to their efficient light absorption (leading to excellent heat conversion efficiencies), ultra-low density (allowing them to be floated on top of the water reservoir), high porosity (enabling water vapor to escape through solar thermal conversion materials) and excellent physico-chemical stability (enabling repeated use).[26] It has been demonstrated by Fu et al. that highly porous GO aerogel membranes have shown good solar thermal heating performance under 3 sun artificial solar irradiation, which allows them to be heated up to about 41 °C (surface temperature) with good thermal conversion efficiencies (~65 %).[22] Further improvements were demonstrated for hybrid GO/CNT/alginate hybrid aerogels by Hu et al., which can reach local temperatures of around 42 °C under only one sun irradiation (1 $kW \cdot m^{-2}$). The resulting aerogel-based solar thermal conversion materials showed solar water evaporation rates of up to 1.62 $kg \cdot m^{-2} \cdot h^{-1}$ under 1 sun irradiation - triple that of pure water under the same irradiation conditions.[21] Similar progresses have been

shown by the work of Huo et al., which uses nitrogen doped graphene aerogels that show a solar thermal conversion efficiencies of up to 90 % and evaporation rates of 1.56 $kg \cdot m^{-2} \cdot h^{-1}$ at 1 $kW \cdot m^{-2}$ solar irradiation.[24]

While the Joule-heating and solar-thermal-heating has been studied and optimized for individual nanocarbon aerogel systems, little is known about the more general inter-relationship between nanocarbon aerogel structure and their electrical or solar-thermal heating properties. In this work, Joule-heating based measurements will be explored as straightforward and reliable methodology to measure heating properties of a broad range of 3D nanocarbon networks. The initial focus in this work will lie on CNT aerogels, produced by polymer-assisted ice-templating (IT)[27] and emulsion-templating (ET)[28] methods, respectively. The as-prepared two nanocarbon aerogels with similar chemistry but fundamentally different microstructure and porosity. The correlation of nanocarbon aerogel structure and heating behavior is then further explored through the investigation of nanocarbon aerogels that differ in nanocarbon building block, density and nanocarbon graphiticity. It is then investigated how the structurally-induced differences impact on the thermal conductivity of the aerogels, and how this is in turn is correlated to the aerogels' functional performance in electrical Joule-heating and solar steam generation.

Results and discussion

In order to study the impact of microstructure on aerogel thermal conductivity, two contrasting CNT aerogels were synthesized via an ice-templating (IT) and emulsion-templating (ET) fabrication approach, respectively (rIT-CNT aerogel and rET-CNT aerogel, as depicted in **Figure 1a**). SEM imaging confirms that the two CNT aerogels exhibit very different internal microstructures (Figure 1b, Figure 1c). While the rIT-CNT aerogel presents some larger, micron-

sized pockets, likely caused by formation of ice-crystals during aerogel synthesis, its primary structural feature is a comparatively dense, continuous 3D network of highly entangled nanotubes (Figure 1c).

In contrast, the internal microstructure of the rET-CNT aerogels consists of emulsion-templated, hollow CNT microspheres, which are relatively loosely packed with large open gaps and channels between them and with a smaller degree of 3D interconnectivity (Figure 1b). SEM indicates that the average size of the gaps and pores in the rET-CNT aerogels is about 5.6 μm (Figure 1d). In contrast, the predominant pore type in the rIT-CNT aerogels stems from the interstitial spaces in the entangled CNT networks, with an average pore size substantially smaller (around 0.1 μm) compared to the rET-CNT aerogel (see also pore size distributions, as measured by image analysis in Figure 1d-1e). The denser, more entangled network microstructure of the rIT-CNT aerogels is further indicated by a high, through-volume electrical conductivity of the aerogel (8.0 S/m, **Table 1**), indicating the presence of a highly interconnected 3D network of high crosslinking density. In contrast, the rET-CNT aerogel exhibits an order-of-magnitude lower through-volume electrical conductivity (0.7 S/m, Table 1), suggesting a lower degree of 3D interconnectivity and crosslinking density, in line with the more open microstructure observed by SEM. The pronounced difference in microstructure is also reflected in other bulk aerogel properties, such as gas permeability (Figure 1g). Through-plane nitrogen flow measurements show highly linear gas velocity-pressure drop correlations (both $R^2 > 0.999$, Figure 1f) that enable to extract the steady-state gas permeability values for both aerogel types (Figure 1g). A distinct difference in gas permeability between the two samples is observed, with the rET-CNT aerogel showing an order-of-magnitude larger nitrogen gas permeability (Figure 1g and Table 1), again consistent with the looser, more open microstructure of the rET-CNT aerogel.

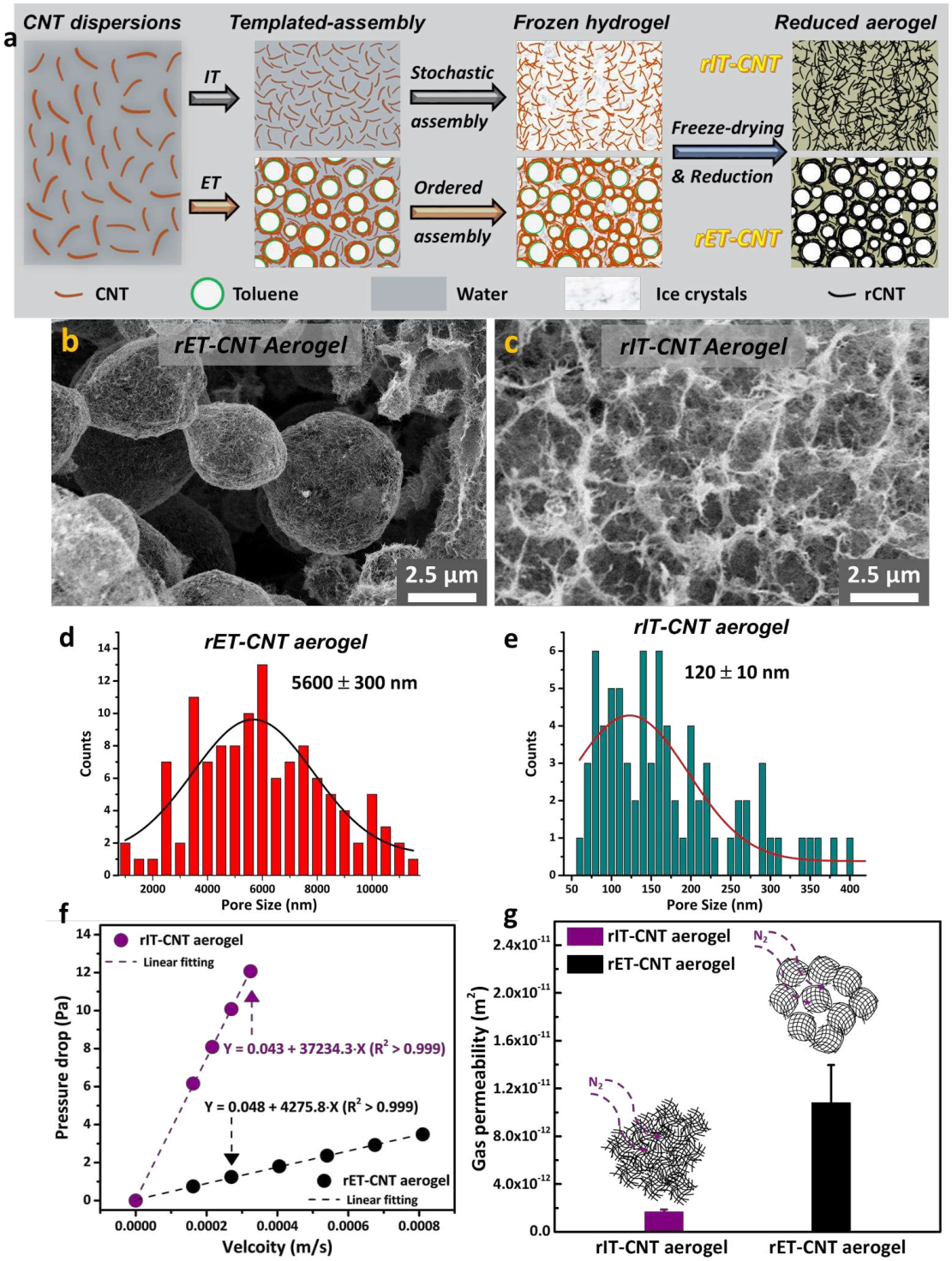

Figure 1. (a) Schematic illustration of the synthesis of nanocarbon aerogels via polymer-assisted ice-templating (rIT-CNT aerogel) and polymer-assisted emulsion-templating (rET-CNT aerogel). (b, c) Microstructure of rET-CNT aerogel and rIT-CNT aerogel as imaged by SEM (sampled from the core region of the monolithic aerogel samples). (d, e) Size distribution of predominant pore type in rET-CNT aerogels and rIT-CNT aerogels, as determined by SEM imaging. (f) Nitrogen gas pressure-drop across the aerogels as function gas velocity for the two aerogels, used to extract through-plane gas permeability values. (g) Through-plane gas permeabilities (in N_2 atmosphere) of the rIT-CNT aerogel and rET-CNT aerogel.

Table 1. Selection of aerogel materials characteristics, that confirm pronounced differences in aerogel microstructure of rET-CNT and rIT-CNT aerogels.

Aerogel	Pore size [a] [μm]	Gas permeability [b] [10^{-11} m^2]	Electrical conductivity, σ [c] [S/m]	Thermal conductivity, κ [d] [$W \cdot m^{-1} \cdot k^{-1}$]
rET-CNT aerogel	5.6	1.08	0.7	0.174
rIT-CNT aerogel	0.1	0.11	8.0	0.104

[a]as obtained from SEM images analysis via Image J; [b]as determined by N_2 gas pressure drop measurements at different gas velocities (see also Figures 1f and 1g); [c]through-volume aerogel electrical conductivity; [d] as determined from radial temperature gradients, measured via aerogel Joule heating at 2W power input (see also Experimental).

In terms of other materials characteristics, the two aerogel samples are however very similar (**Table 2**). Both aerogels are formed from the same MWCNT raw material using the same polymer-assisted approach, with the only modification occurring in the templating agent which is completely removed in both cases during the final high-temperature annealing step (see Experimental). The two aerogels are therefore very similar in their basic crosslinking chemistry, i.e. they are both aerogels based on covalent crosslinking through graphitized polymer residues formed during the annealing step.[29] Furthermore, both aerogels show very similar, high thermal stability to temperatures up to 555 °C,[30] even in oxidative air atmosphere, which is an important requisite for many practical thermal applications of nanocarbon aerogels and for the heating experiments conducted in this work (see ESI Figure S1, Table 2). Raman spectra and XRD patterns of the aerogels confirm also very similar graphitic crystallinity and defect concentrations of the CNTs in the aerogels (see ESI Figure S2-S3, Table 2).[29, 31] Nitrogen absorption measurements show that the specific surface areas are also relatively similar, with the surface area of the rET-CNT aerogel only around 20 % different from the rIT-CNT aerogels (see ESI Figure S4, Table 2). The main distinguishing feature between the rIT-CNT and rET-CNT aerogels is therefore their highly contrasting internal structure, making the samples an interesting first model

system to investigate Joule-heating characteristics as function of nanocarbon aerogel microstructure.

Table 2. Physico-chemical materials characteristics of rET-CNT aerogel and rIT-CNT aerogel.

Aerogel	Nano-carbon type	Envelope Density [a] [g/cm^3]	Combustion Temperature [b] [°C]	Specific Surface Area [c] [m^2/g]	graphitic crystal domain size [d] [nm]	Raman I_D/I_G ratio [e]
rET-CNT aerogel	rCNT	0.006	555 °C	358	2.23	0.75
rIT-CNT aerogel	rCNT	0.009	555 °C	290	2.44	0.82

[a]ρ represents aerogel envelope density; [b]Nanocarbon combustion temperature, as obtained by TGA in air (see also ESI, Figure S1); [c]specific surface area as obtained by BET analysis (see also ESI, Figure S4); [d]crystal domain size along the stacking direction of the graphitic layers, as estimated from the graphitic (002) XRD peak (see also ESI, Figure S3); [e] Raman I_D/I_G ratio (see also ESI, Figure S2).

In order to quantitatively measure Joule-heating characteristics, electrical measurements of the aerogels were carried out using a custom-made Joule-heating set-up (**Figure 2a** and ESI Figure S5). All samples were investigated after careful preconditioning at 200 °C (see Experimental) to remove adsorbents (water, ambient volatile impurities) from the nanocarbon surfaces, in order to ensure repeatability of the Joule-heating measurements (see ESI Figure S6-S7). After preconditioning, both aerogels show highly linear I-U characteristics up to currents of 0.5 A and voltages of 20 V, confirming that the aerogels behave as Ohmic resistors over the current-voltage range investigated (see ESI Figure S8). In the current-voltage range studied here, resistive aerogel Joule-heating to temperature up to 185 °C is observed. Over this temperature range, the aerogels show only relatively minor changes in electrical resistivity (less than 20 % change between room temperature and 185 °C, Figure 2b). Interestingly, aerogel resistivity decreases with increasing temperature, indicating a semiconductor-type behavior (in contrast to the metallic nature of individual MWCNTs),[32] potentially originating from junction resistance effects in the 3D networks and/or incomplete graphitization of polymer residues during the thermal treatment step.

To assess heating efficiency the steady state Joule-heating temperatures of the aerogels were measured at different electrical power inputs (P = I × V, Figure 2c and **Table 3**). The resulting Joule-heating plots indicate substantial differences in Joule-heating efficiency (here defined as temperature increase per electrical power input, dT/dP). Specifically, the rIT-CNT aerogel exhibits a more than 60 % larger Joule-heating efficiency (74 ^{o}C/W) compared to the rET-CNT aerogel (46 ^{o}C/W). This efficiency difference is confirmed by Joule-heating experiments carried out at constant electrical power input. For example, at the same electrical power input of 2W, the rIT-CNT aerogel reaches a significantly higher Joule-heating core temperature (168 ± 8°C, Table 3) compared to the rET-CNT aerogels (114 ± 4°C, Table 3). The stability and repeatability of the aerogels' Joule-heating characteristics under these temperature conditions is evidenced by highly repeatable Joule-heating cycling (Figure 2d). Differences are also observed for the rate of Joule-heating of the two aerogel samples. When monitoring Joule-heating temperature over time after 'switching-on' an electrical heating current (set to a consistent power input of 2W), both aerogels show extremely fast heating kinetics (up to 300 °C/min), with the rET-CNT aerogels showing slightly faster Joule-heating compared to the rIT-CNT aerogels (Figure 2e, Table 3, ESI Figure S9). Due to the excellent thermal conductivity of the nanocarbon framework, both aerogels also cool down to room temperature extremely fast once the electrical heating current has been 'switched-off' (cooling rates of up to 320 °C/min, Figure 2f, ESI Figure S9). Cooling kinetics for the rET-CNT aerogel are about 20 % faster compared to the rIT-CNT aerogel (Table 3), potentially caused by the more open internal microstructure, promoting heat loss during cooling.[11] The significant differences in heating efficiencies and kinetics clearly demonstrate that aerogel microstructure is a key factor impacting resistive heating behavior.

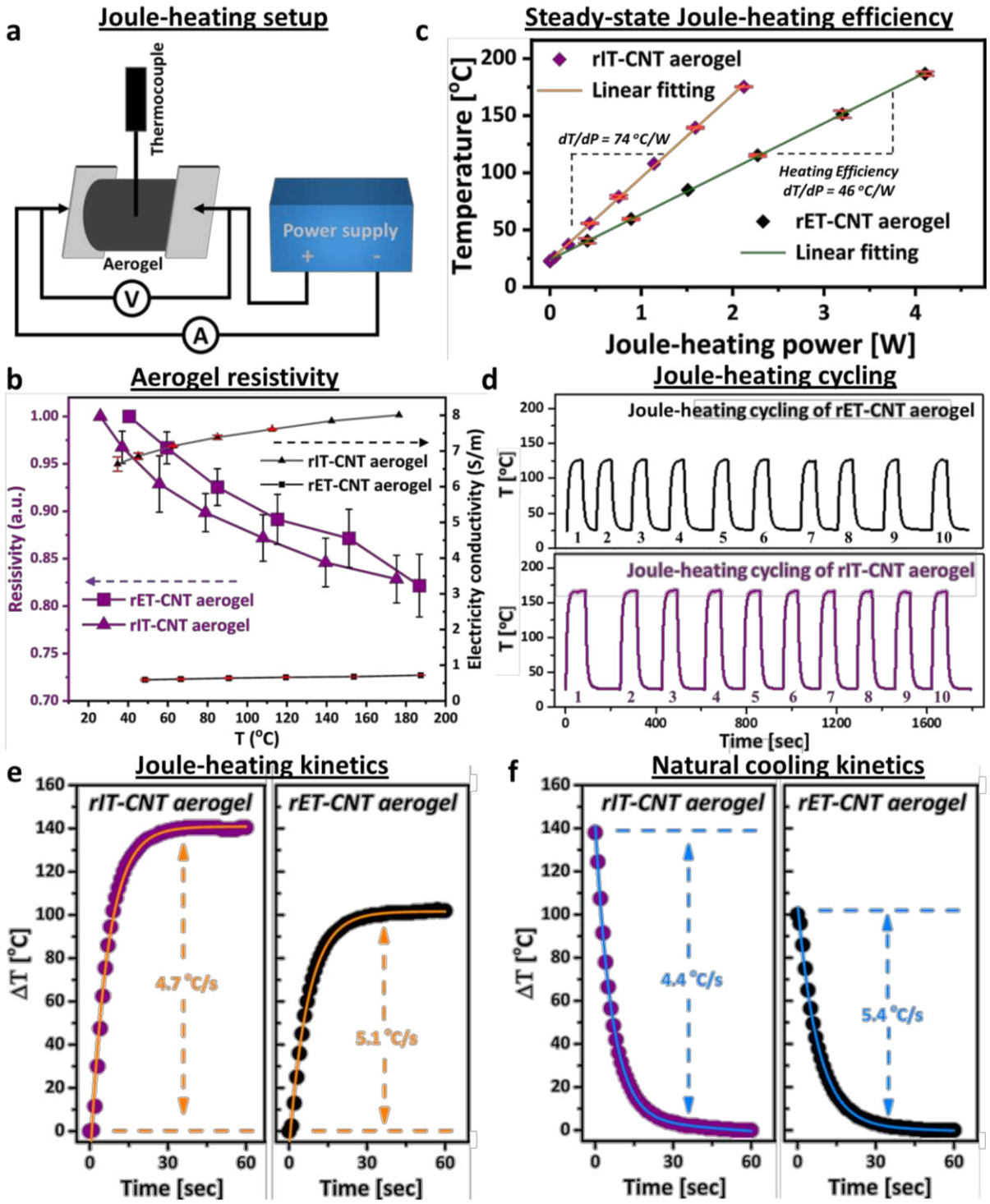

Figure 2. (a) Schematic of a nanocarbon aerogel Joule-heating setup. (b) Electrical properties of rET-CNT and rIT-CNT aerogels: electrical conductivity and relative resistivity as function of Joule-heating temperature. (c) Joule-heating characterization of rET-CNT and rIT-CNT aerogels via current-step experiments: steady-state Joule-heating core temperature as function of electrical power input. (d) Joule-heating cycling of rET-CNT and rIT-CNT aerogels at 2W. (e) Joule-heating kinetics: increase in aerogel core temperature with time (2W electrical power input switched on at t = 0 sec); (f) Natural cooling kinetics: decrease of aerogel core temperature with time (2 W electrical power input switched off at t = 0 sec).

Table 3. Joule-heating characteristics of rET-CNT aerogel and rIT-CNT aerogel collected at a heating power 2W.

Aerogel	Core Temperature T [ºC]	Heating Efficiency dT/dP [°C/W]	Heating Rate dT/dt [°C/min]	Cooling Rate -dT/dt [°C/min]
rET-CNT aerogel	114	46	306	324
rIT-CNT aerogel	168	75	282	264

It is most likely that microstructure differences of the aerogels result in a difference of their thermal conductivities, which then strongly influenced the heating performances. Thermal conductivity will control heat transfer and therefore heat losses to the environment, and therefore directly impact on steady-state Joule-heating temperature.[11, 33, 34] To measure the thermal conductivity of the aerogels, the radial temperature gradient of Joule-heated aerogels was analyzed. Specifically, the temperature decline of a Joule-heated aerogel from the aerogel core to the outer surface is measured and the resulting radial gradient used to estimate the thermal conductivity (see also Experimental and ESI Figure S10). It has been shown that this approach provides values in good agreement with thermal conductivity values, determined by other methods, such as thermal diffusivity-based approaches.[11] For the two CNT aerogels studied here, the thermal conductivity of the rIT-CNT aerogel is found to be about 70 % smaller than that of the rET-CNT aerogel, likely resulting in reduced heat losses to the environment and therefore overall higher Joule-heating efficiency for the rIT-CNT aerogel. To further confirm this controlling effect of thermal conductivity, a series of four additional ice-templated aerogels were synthesized. The ice-templating synthesis was modified by changing nanocarbon building block (CNT replaced by GO, sample labelled as rIT-GO aerogel) and thermal reduction treatment (change of reduction atmosphere to N_2 and reduction temperature to 800 °C; samples labelled as rIT-CNT_{N2}, rIT-GO_{N2}

and rIT-GO_{800} aerogel respectively). All samples were then characterized in terms of envelope density, electrical conductivity, and thermal conductivity (**Table 4**, ESI Figure S11-S14).

Table 4. Conductivity and Joule-heating characteristics of other ice-templated nanocarbon aerogels.

Aerogel	$\rho^{a)}$ [mg/cm^3]	$\sigma^{b)}$ [S/m]	$\kappa^{c)}$ [W·m^{-1}·k^{-1}]	T $^{d)}$ [^{o}C]	dT/dP $^{e)}$ [°C/W]
rIT-GO aerogel	4.9	8.9	0.152	116	48
rIT-CNT_{N2} aerogel	9.8	7.3	0.135	136	57
rIT-GO_{N2} aerogel	6.4	5.7	0.156	113	46
rIT-GO_{800} aerogel	6.3	9.6	0.125	143	61

[a)]aerogel envelope density; [b)]through-volume aerogel electrical conductivity; [c)]thermal conductivity, as determined from radial temperature gradients, measured via aerogel Joule heating at 2W power input; [d)]Joule-heating temperature at aerogel core, obtained at a heating power of 2W; [e)]Joule-heating efficiency, as determined from current step experiments.

Joule-heating experiments of these additional aerogel samples at an electrical power input of 2W were used to measure steady-state Joule-heating characteristics. As expected, the four additional aerogels show clear differences in Joule-heating efficiency. However, their Joule-heating efficiencies do not correlate with key aerogel characteristics, such as electrical conductivity or envelope density (**Figure 3a** and Figure 3b). However, a very clear correlation emerges when Joule-heating efficiency is plotted as function of thermal conductivity (Figure 3c). The inversely proportional relationship between thermal conductivity and Joule-heating efficiency described above is confirmed and can be qualitatively explained by reduced heat transfer into the environment in aerogels with lower thermal conductivity.[35] The origin for the linear nature of this relationship is not fully clear and requires future investigations. Nevertheless, these findings very clearly demonstrate that thermal conductivity is a key factor in determining Joule-heating characteristics of nanocarbon aerogels. In order to increase Joule-heating efficiency for heating applications (local gas heaters, thermal sorbent regeneration, thermal de-freezing materials),[4, 35, 36] nanocarbon aerogels with relatively low thermal conductivities (here observed for aerogels with

denser network structure and high crosslinking density) are likely beneficial. In contrast, for applications where Joule-heating effects need to be minimized (e.g. catalytic supports in fuels cells, battery materials etc.),[5, 37] nanocarbon materials with relatively high thermal conductivity (here observed for aerogels with open microstructure and large pore sizes) are likely a better choice.

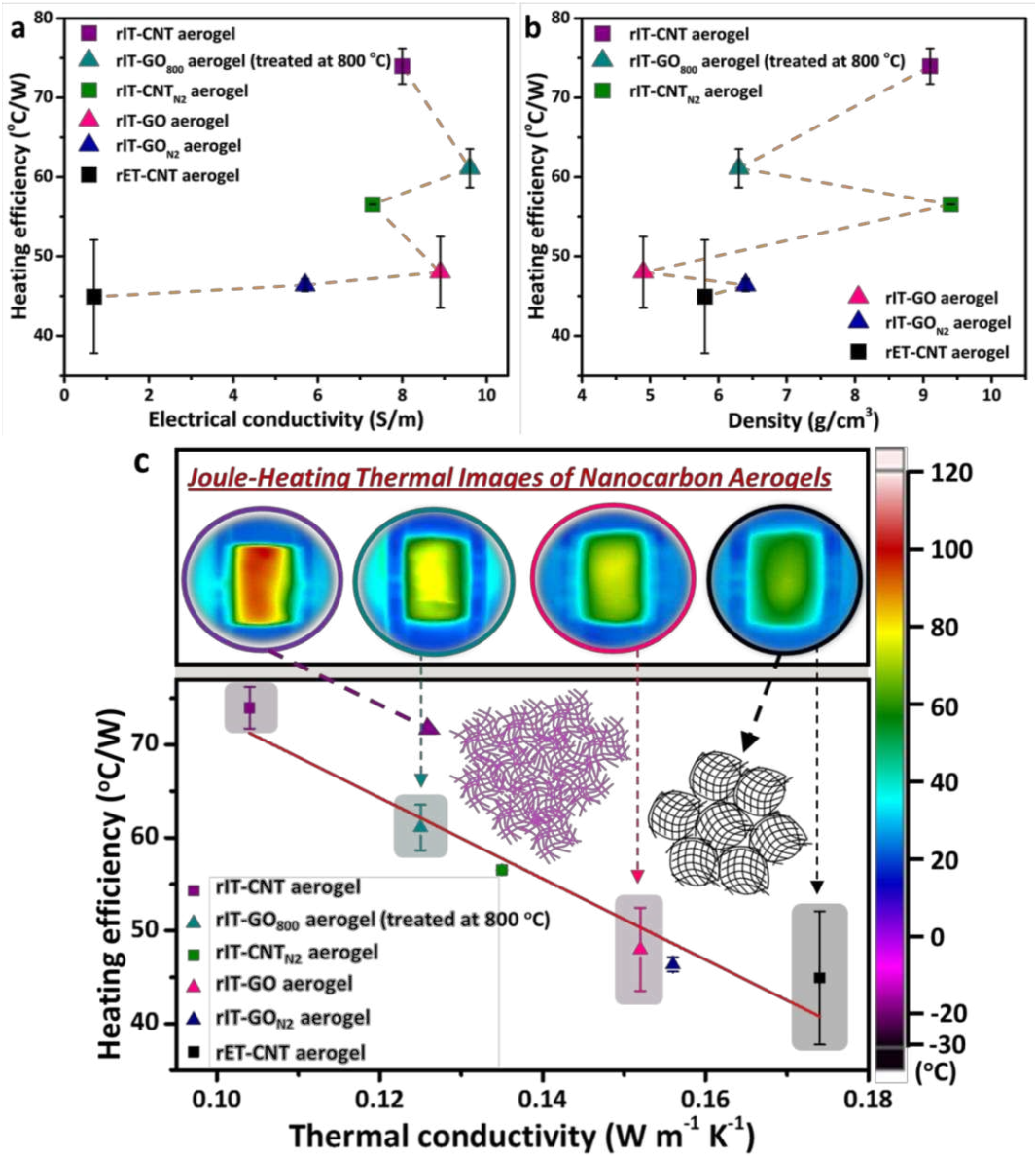

Figure 3. Correlation of aerogel Joule-heating efficiency with different physico-chemical aerogel characteristics. (a) Plot of Joule-heating efficiency vs. aerogel electrical conductivity, (b) Plot of Joule-heating efficiency vs. aerogel envelope density. (c) Linear correlation between Joule-heating efficiency and aerogel thermal conductivity (Inserted thermal images show aerogel surface temperatures at 2W electrical power input).

Differences in thermal aerogel conductivity are also important to tailor functional performance of nanocarbon aerogels in other heating-related applications. As an example, the rET-CNT aerogel and rIT-CNT aerogel were investigated as solar thermal conversion materials (STCM) for solar steam generation applications. Like other nanocarbon aerogels reported in the literature, our rET-CNT and rIT-CNT aerogels exhibit excellent STCM characteristics. Both aerogels show highly efficient light absorption across the whole solar spectrum (more than that 94 % absorbance between 200 nm to 2000 nm), ensuring high solar thermal conversion efficiencies (**Figure 4a**).[21] Contact angle measurements indicate an overall similar, hydrophobic surface character (see ESI Figure S15). While light absorption and surface character are very similar in both aerogels, they exhibit significantly different thermal conductivities (60 % higher thermal conductivity for the rET-CNT aerogel), as discussed above. To assess the impact of this difference on solar heating, cylindrical rET-CNT and rIT-CNT aerogels were placed on a glass surface and heated through light irradiation from the top (one sun solar simulator, see Figure 4b). Upon reaching steady state, the temperature of the aerogels was then thermally imaged perpendicular to the irradiation direction (Figure 4b inset). The resulting thermal images were analyzed via line scans to plot the temperature gradient from the irradiated aerogel top towards the non-irradiated aerogel bottom (Figure 4b). The temperature of the irradiated aerogel top reaches up to 46 °C, comparable to other nanocarbon based aerogels reported in the literature.[21] The 'vertical' temperature gradient between aerogel top and bottom is shallower and plateaus at a higher temperature for the rIT-CNT aerogel. This effect is a direct consequence of the lower thermal conductivity of the rIT-CNT aerogel, resulting in reduced heat dissipation, and hence more effective trapping of solar heat.

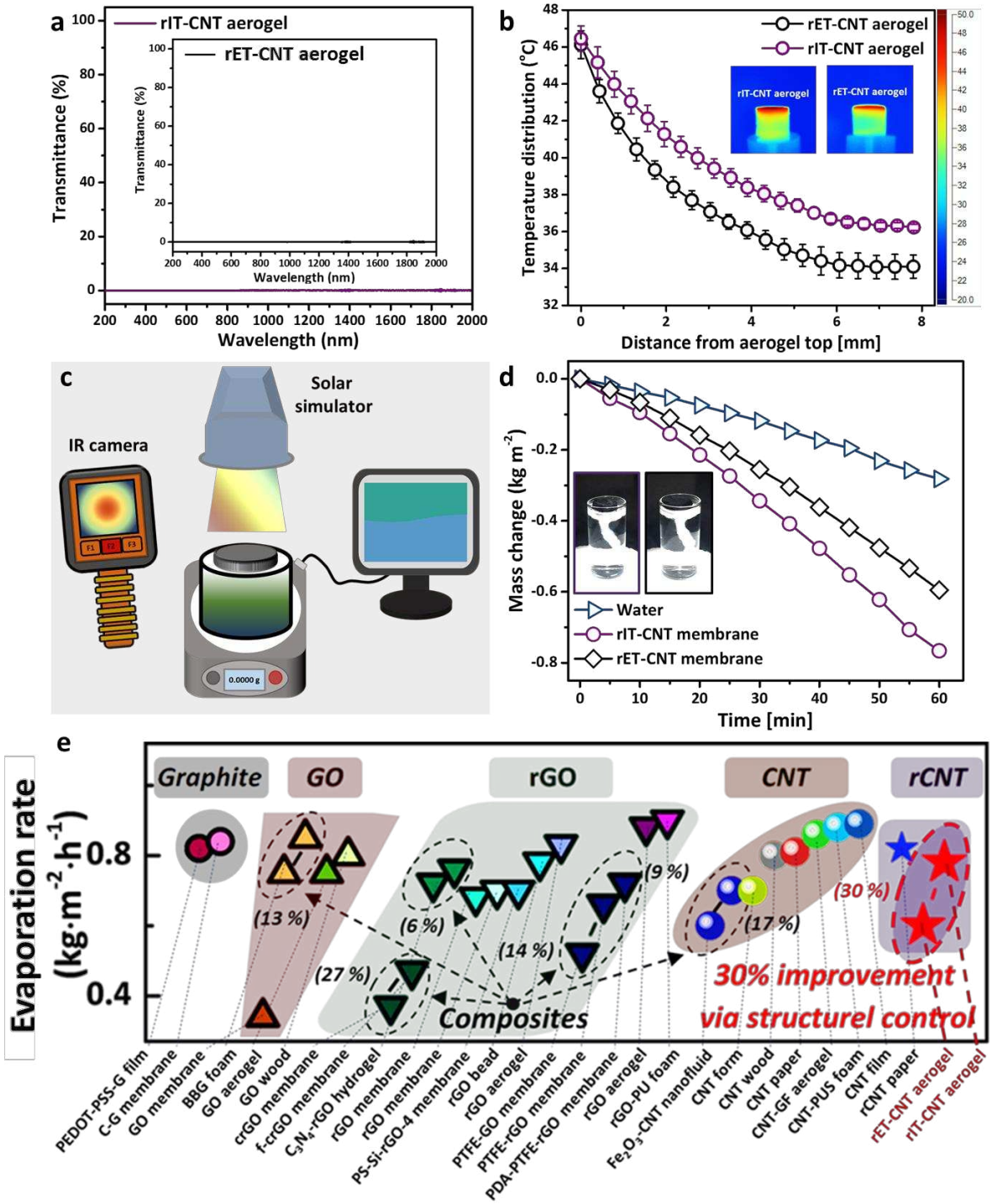

Figure 4. (a) Solar absorption of rIT-CNT aerogel and rET-CNT aerogel. (b) Decline of solar-thermal heating temperature from the aerogels' top surface towards aerogels' bottom surface at 1 sun solar irradiation (aerogels illuminated from the top). (c) Setup for solar steam generation experiments, using rCNT aerogel membranes over a water reservoir. (d) Solar steam generation performance of rET-CNT and rIT-CNT aerogels under one sun irradiation: Water mass change (normalized to surface area of water reservoir) over time for pure water, water with rIT-CNT aerogel, and water with rET-CNT aerogel (Insert shows digital photos of aerogel membranes on top of water reservoir). (e) Solar steam water evaporation rates of different nanocarbon-based solar evaporators under one sun illumination, reported in the literature.

To further investigate this effect, the membrane-shaped aerogels were tested for solar steam generation. Membrane-shaped rET-CNT and rIT-CNT aerogels were fabricated using the exact same synthetic parameters as used before, but using smaller volumes of nanocarbon dispersions.[38] For the solar steam evaporation experiment, the aerogel membranes were floated on a water reservoir, irradiated from the top, and the resulting weight loss due to water evaporation monitored through a computer-controlled balance (Figure 4c). Monitoring water evaporation under one sun irradiation shows that the rIT-CNT aerogel exhibits indeed the best solar steam generation performance at a water evaporation rate of 0.78 $kg \cdot m^{-2} \cdot h^{-1}$, i.e. 30 % higher water evaporation efficiency than that of the rET-CNT aerogel and three times higher than that of pure water (Figure 4d). In terms of absolute values, these evaporation rates are comparable to many carbon-based solar thermal conversion materials reported in the literature (Figure 4e, ESI Table S1).[22, 27, 39-58] Higher water evaporation rates of more than 1 $kg \cdot m^{-2} \cdot h^{-1}$ (like those mentioned in the introduction) are typically achieved through further chemical functionalization of the aerogels (e.g. functionalization with alginate or nitrogen doping)[21, 24] which facilitates the transport of water vapor through the aerogel material. However, our findings clearly show that tailoring the physical microstructure of the aerogel material is an important additional tool to increase solar evaporation efficiencies by at least 30 % as demonstrated here. As observed in the solar steam experiments, the best solar thermal heating efficiencies are observed for the rIT-CNT, i.e. the aerogel with the lower thermal conductivity.

Conclusions

In this work, ice-templating and emulsion-templating approaches were used to form two types of aerogels consisting of CNT 3D networks (rIT-CNT aerogel and rET-CNT aerogel), which have

contrasting internal structures and display very different Joule-heating performance. By tuning aerogel microstructure, porosity, and graphiticity and systematically measuring their Joule-heating characteristics (steady-state core temperatures, Joule-heating kinetics), we show that the Joule-heating efficiencies of the materials are highly correlated with their thermal conductivities. In our systematic set of samples, the lowest thermal conductivity and therefore highest Joule-heating efficiency was displayed by the rIT-CNT aerogel, structurally based on a combination of a more dense, interconnected microstructure and relatively small pore size. Importantly, the principles we discovered are transferable to solar steam generation, where the rIT-CNT aerogel displays a 30% higher water evaporation efficiency than the rET-CNT aerogel under one sun light exposure. The principles we discovered can guide the design of 3D nanocarbon aerogel networks for a wide range of applications, including gas heater, clean water generation or Joule-heating-assisted nanoparticle absorption/desorption.

Experimental and Methods

Materials: Carboxylic acid functionalized multi-wall carbon nanotubes (CNT, avg. diam. × L, 9.5 nm ×1.5 μm) and polyvinyl alcohol (PVA, Mw: 85000-124000) were purchased from Sigma-Aldrich. Graphene oxide (GO, 0.3 - 0.7 cm diam., carbon: 65-75%, oxygen > 18%, nitrogen < 1%, sulfur < 2%) flakes were purchased from William Blythe Limited. Sucrose, toluene, hydrochloride acid and HPLC were purchased from Scientific UK. All chemicals were used without further purification.

Templated syntheses of nanocarbon aerogels (rIT-CNT, rIT-GO and rET-CNT): Ice-templated nanocarbon aerogels were synthesized via a polymer-assisted procedure as shown in Figure 1a (top row of schematics). Specifically, 0.0375 g PVA and 0.0375 g sucrose were

dissolved in 10 mL HPLC water via tip-probe sonication 10 minutes (30% of ultrasound power, model HD2200, Bandelin sonopuls). Then, 0.075 g nanocarbons (CNT or GO starting materials) were added into above mixtures and sonicated 4 times to ensure a high degree of nanocarbon exfoliation (each sonication duration 5 minutes). After each sonication, the nanocarbon mixtures were vigorously agitated for at least 3 minutes to uniformly mix the dispersion (3000 rpm/min). After that, 3.5 mL of the mixtures were added into a bespoke PTFE cylindrical module (I.D. 18 mm, O.D. 20 mm, height 20 mm), followed by freezing in liquid nitrogen and freeze-drying for 24 hours (LABCONCO freeze dryer). The obtained non-reduced nanocarbon aerogels were thermally reduced at 1000 ^{o}C for 2 hours in H_2/N_2 (5% H_2) atmosphere with a heating rate of 5 ^{o}C/min (Carbolite Gero Limited). Final thermally reduced samples are referred to as rIT-GO aerogel and rIT-CNT aerogel, respectively.

A polymer-assisted emulsion-templating approach was employed to prepare a second type of nanocarbon aerogel, with fundamentally different porosity (rET-CNT aerogel, Figure 1a lower row of schematics). An initial aqueous CNT/PVA/sucrose dispersion was prepared using the same synthetic parameters employed for the rIT-CNT aerogel. Then, 2.5 mL toluene were added to this initial aqueous CNT dispersion, followed by the addition of 1 mL 0.1M HCl under agitation to induce the formation of CNT-stabilized water/toluene emulsion. The resulting emulsion was then frozen, freeze-dried and thermally reduced, using the same parameters used for the rIT-CNT aerogel. In order to produce aerogels with different degree of chemical reduction, IT-GO aerogels were reduced in H_2/N_2 atmosphere at a temperature of 500 ^{o}C and 800 ^{o}C (samples labeled as rIT-GO_{500} aerogels and rIT-GO_{800} aerogels, respectively), as well as in pure N_2 atmosphere at 1000 °C (labelled as rIT-CNT_{N2} aerogel and rIT-GO_{N2} aerogel). All the IT and ET aerogels were fabricated

into the same cylindrical shape and size (diameter ~1.6 cm, height ~1.3 cm), important to reduce error in Joule-heating based property measurements.

Joule-heating measurements: In order to Joule-heat aerogels in a highly controlled manner, the cylindrical aerogel monoliths were inserted into a custom-made, electrically-contactable sample holder (Figure 2a, ESI Figure S5), consisting two circular, aluminum electrodes, held by two moveable, heat-resistant alumina holding blocks. A DC power supply was then connected to the electrodes and was used to control electrical current through the aerogel sample. The current-induced Joule-heating of the aerogel was measured using a thin (0.25 mm diameter) K-type thermocouple (TJC 120 Series, TJC120-CASS-IM025U-250-HMPW-M, Omega UK), inserted into the aerogel core, using a data logger (EL-USB-TC, Lascar Electronics) for continuous temperature read out. To visualize the aerogels' surface temperature a thermal IR camera (Model: Fluke TiR1) was used. All aerogel samples were preconditioned at a Joule-heating temperature of 200 ºC for 20 minutes to remove adsorbed water and gases. Then current-step experiments were carried out by stepwise increasing electrical current and, hence, Joule-heating temperature of the aerogel samples. At each step, the current was kept constant for 10 minutes before switching to the next current step (see ESI Figure S6-S7). These current-step experiments were used to measure the aerogels' Joule-heating response at different electrical power inputs.

Measurement of aerogel thermal conductivity through Joule-heating experiments: At constant electrical current input, the Joule-heating temperature of an aerogel at the aerogel core will be considerably higher than at the aerogel surface due to constant heat loss at the aerogel surface. The difference between the monolith core and surface temperature (i.e. the degree of heat loss) is crucially dependent on the thermal conductivity of the aerogel. The radial core-to-surface

temperature gradient (Figure S10 for representative data from this work) can be analyzed by a simplified model for one-dimensional heat conduction in cylinders with homogeneous, internal energy generation[11]:

$$T=C_{rad}\cdot r^2+T_{surf} \qquad \text{(Equation 1)}$$

$$\kappa=q/(4\cdot C_{rad}) \qquad \text{(Equation 2)}$$

where r is the distance from the aerogel core (mm); T is the measured temperature at distance r (^oC); q is the Joule-heating energy density (W/m^3); T_{surf} is the surface temperature; C_{rad} is the corresponding quadratic fit parameters (K/m^2); κ is the thermal conductivity of the aerogel ($W\cdot m^{-1}\cdot K^{-1}$), and q is the Joule-heating energy density (W/m^3, estimated as ratio of electrical power input over aerogel monolith volume).[11] To determine aerogel thermal conductivity, the radial Joule-heating gradients of cylindrical aerogels (diameter ~1.6 cm, height ~1.3 cm) were determined at an electrical power input of 2W, measuring Joule-heating temperatures at different radial distances from the aerogel core via a thermal couple. Thermal conductivity values were extracted from the resulting temperature gradient plots through quadratic fitting (Equations 1 and 2). All Joule-heating experiments were carried out at least three times and exhibited high reproducibility.

Material characterization: Thermogravimetric analysis (TGA) was measured in air atmosphere to analyze the thermal stability of nanocarbon aerogels, using 10 ^oC/min ramping rate from 20 to 850 ^oC (TGA Q600 model, USA). Brunauer-Emmett-Teller (BET) surface area measurements were conducted using a Micromeritics TriStar 3000 instrument. All measured samples were degassed under N_2 gas atmosphere at 110 ^oC for 3 hours prior to analysis. Scanning electron microscopy (SEM) images were taken using a Nova NanoSEM 450 with an accelerating voltage

of 3 kV. Thermal images were taken using Fluke TiR1 thermal camera and were analyzed via Fluke Connect software. Raman spectra were measured using a Renishaw InVia with an excitation laser wavelength of 532 nm between 400 and 4000 cm^{-1}. X-ray diffraction (XRD) was conducted on a Bruker D2 Phaser Diffractometer. The through-plane gas permeability of nanocarbon aerogels was tested using an in-house built setup with a flow controller (HFC-202, Teledyne Hastings, UK) and a differential pressure sensor (PX653, Omega, UK). The gas permeability value (K) of the measured aerogel sample was calculated via the following equation, $K = (\mu \cdot m)/S$, where K is the gas permeability (m^2), μ is the dynamic viscosity value of nitrogen (1.80×10^{-5} Pa·s), m is the thickness of the aerogel samples (m), and S is the extracted slope ($Pa \cdot s \cdot m^{-1}$) from Figure 1f. Aerogel light absorption (wavelength range from 200 nm to 2000 nm) was measured using a UV/VIS/NIR spectrometer (Lambda 950, PerkinElmer). Static water contact angles were tested using a drop-shape analysis device (OCA 25, Dataphysics UK). Solar steam generation was measured using a solar simulator (Newport Co.) under 1 sun solar radiation, using a digital balance (uncertainty of ± 0.001 g, Ohaus, Mettler Toledo) to measure the mass change over time.

Corresponding Author

* Dong Xia, Email: cmdx@leeds.ac.uk, Tel: +44(0)7596218478

Notes

The authors declare no competing financial interest.

Supporting Information

Detailed Joule-heating measurements and solar-thermal heating data of nanocarbon aerogels can be found in the Supporting Information.

Acknowledgements

The authors would appreciate the China Scholarship Council and University of Leeds for the funding supports. The research of YX was supported by a Leverhulme research project grant (RPG-2017-178), and the Marie Curie Individual Fellowship (H2020-MSAC-IF-2019-885795-PolyTEM).

References

1. Wan, W.; Zhang, R.; Li, W.; Liu, H.; Lin, Y.; Li, L.; Zhou, Y., Graphene-carbon nanotube aerogel as an ultra-light, compressible and recyclable highly efficient absorbent for oil and dyes. *Environ. Sci. Nano* **2016**, *3*, 107-113.
2. Lu, K. Q.; Xin, X.; Zhang, N.; Tang, Z. R.; Xu, Y. J., Photoredox catalysis over graphene aerogel-supported composites. *J. Mater. Chem. A* **2018**, *6*, 4590-4604.
3. Xia, D.; Li, H.; Mannering, J.; Huang, P.; Zheng, X.; Kulak, A.; Baker, D.; Iruretagoyena, D.; Menzel, R., Electrically heatable graphene aerogels as nanoparticle supports in adsorptive desulfurization and high-pressure CO_2 capture. *Adv. Funct. Mater.* **2020**, *30*, 2002788.
4. Xia, D.; Li, H.; Huang, P.; Mannering, J.; Zafar, U.; Baker, D.; Menzel, R., Boron-nitride/carbon-nanotube hybrid aerogels as multifunctional desulfurisation agents. *J. Mater. Chem. A* **2019**, *7*, 24027-24037.
5. Mao, J.; Iocozzia, J.; Huang, J.; Meng, K.; Lai, Y.; Lin, Z., Graphene aerogels for efficient energy storage and conversion. *Energ. Environ. Sci.* **2018**, *11*, 772-799.
6. Yavari, F.; Chen, Z.; Thomas, A. V.; Ren, W.; Cheng, H. M.; Koratkar, N., High sensitivity gas detection using a macroscopic three-dimensional graphene foam network. *Sci. Rep.* **2011**, *1*, 1-5.
7. Yang, Y.; Zhao, R.; Zhang, T.; Zhao, K.; Xiao, P.; Ma, Y.; Ajayan, P. M.; Shi, G.; Chen, Y., Graphene-based standalone solar energy converter for water desalination and purification. *ACS Nano* **2018**, *12*, 829-835.
8. Ren, H.; Tang, M.; Guan, B.; Wang, K.; Yang, J.; Wang, F.; Wang, M.; Shan, J.; Chen, Z.; Wei, D., Hierarchical graphene foam for efficient omnidirectional solar-thermal energy conversion. *Adv. Mater.* **2017**, *29*, 1702590.
9. Liu, L.; Yang, X.; Lv, C.; Zhu, A.; Zhu, X.; Guo, S.; Chen, C.; Yang, D., Seaweed-derived route to Fe_2O_3 hollow nanoparticles/N-doped graphene aerogels with high lithium ion storage performance. *ACS Appl. Mater. Inter.* **2016,** *8*, 7047-7053.

10. Liang, W.; Wang, B.; Cheng, J.; Xiao, D.; Xie, Z.; Zhao, J., 3D, eco-friendly metal-organic frameworks@carbon nanotube aerogels composite materials for removal of pesticides in water. *J. Hazard. Mater.* **2020,** *401*, 123718.
11. Menzel, R.; Barg, S.; Miranda, M.; Anthony, D. B.; Bawaked, S. M.; Mokhtar, M.; Al-Thabaiti, S. A.; Basahel, S. N.; Saiz, E.; Shaffer, M. S. P., Joule heating characteristics of emulsion-templated graphene aerogels. *Adv. Funct. Mater.* **2015**, *25*, 28-35.
12. Hu, P.; Lyu, J.; Fu, C.; Gong, W. B.; Liao, J.; Lu, W.; Chen, Y.; Zhang, X., Multifunctional aramid nanofiber/carbon nanotube hybrid aerogel films. *ACS Nano* **2019**, *14*, 688-697.
13. Qin, D. D.; Zhu, Y. J.; Chen, F. F.; Yang, R. L.; Xiong, Z. C., Self-floating aerogel composed of carbon nanotubes and ultralong hydroxyapatite nanowires for highly efficient solar energy-assisted water purification. *Carbon* **2019**, *150*, 233-243.
14. Mu, P.; Zhang, Z.; Bai, W.; He, J.; Sun, H.; Zhu, Z.; Liang, W.; Li, A., Superwetting monolithic hollow-carbon-nanotubes aerogels with hierarchically nanoporous structure for efficient solar steam generation. *Adv. Energy Mater.* **2019**, *9*, 1802158.
15. Wang, K.; Zeng, Y.; Lin, W.; Yang, X.; Cao, Y.; Wang, H.; Peng, F.; Yu, H., Energy-efficient catalytic removal of formaldehyde enabled by precisely joule-heated Ag/Co_3O_4@ mesoporous-carbon monoliths. *Carbon* **2020**, *167*, 709-717.
16. Mas, B.; Fernández-Blázquez, J. P.; Duval, J.; Bunyan, H.; Vilatela, J. J., Thermoset curing through Joule heating of nanocarbons for composite manufacture, repair and soldering. *Carbon* **2013**, *63*, 523-529.
17. Xia, T.; Zeng, D.; Li, Z.; Young, R. J.; Vallés, C.; Kinloch, I. A., Electrically conductive GNP/epoxy composites for out-of-autoclave thermoset curing through Joule heating. *Compos. Sci. Technol.* **2018**, *164*, 304-312.
18. Wang, C.; Ping, W.; Bai, Q.; Cui, H.; Hensleigh, R.; Wang, R.; Brozena, A. H.; Xu, Z.; Dai, J.; Pei, Y., A general method to synthesize and sinter bulk ceramics in seconds. *Science* **2020**, *368*, 521-526.
19. De Villoria, R. G.; Yamamoto, N.; Miravete, A.; Wardle, B. L., Multi-physics damage sensing in nano-engineered structural composites. *Nanotechnology* **2011**, *22*, 185502.
20. Ge, J.; Shi, L. A.; Wang, Y. C.; Zhao, H. Y.; Yao, H. B.; Zhu, Y. B.; Zhang, Y.; Zhu, H. W.; Wu, H. A.; Yu, S. H., Joule-heated graphene-wrapped sponge enables fast clean-up of viscous crude-oil spill. *Nat. Nanotechnol.* **2017**, *12*, 434-440.
21. Hu, X.; Xu, W.; Zhou, L.; Tan, Y.; Wang, Y.; Zhu, S.; Zhu, J., Tailoring graphene oxide-based aerogels for efficient solar steam generation under one sun. *Adv. Mater.* **2017**, *29*, 1604031.
22. Fu, Y.; Wang, G.; Mei, T.; Li, J.; Wang, J.; Wang, X., Accessible graphene aerogel for efficiently harvesting solar energy. *ACS Sustain. Chem. Eng.* **2017**, *5*, 4665-4671.
23. Fu, Y.; Wang, G.; Ming, X.; Liu, X.; Hou, B.; Mei, T.; Li, J.; Wang, J.; Wang, X., Oxygen plasma treated graphene aerogel as a solar absorber for rapid and efficient solar steam generation. *Carbon* **2018,** 130, 250-256.
24. Huo, B.; Jiang, D.; Cao, X.; Liang, H.; Liu, Z.; Li, C.; Liu, J., N-doped graphene/carbon hybrid aerogels for efficient solar steam generation. *Carbon* **2018**, *130*, 250-256.
25. Wang, Z.; Horseman, T.; Straub, A. P.; Yip, N. Y.; Li, D.; Elimelech, M.; Lin, S., Pathways and challenges for efficient solar-thermal desalination. *Sci. Adv.* **2019**, *5*, eaax0763.
26. Deng, Z.; Zhou, J.; Miao, L.; Liu, C.; Peng, Y.; Sun, L.; Tanemura, S., The emergence of solar thermal utilization: solar-driven steam generation. *J. Mater. Chem. A* **2017**, *5*, 7691-7709.

27. Wang, G.; Fu, Y.; Guo, A.; Mei, T.; Wang, J.; Li, J.; Wang, X., Reduced graphene oxide-polyurethane nanocomposite foam as a reusable photoreceiver for efficient solar steam generation. *Chem. Mater.* **2017**, *29*, 5629-5635.
28. Barg, S.; Perez, F. M.; Ni, N.; do Vale Pereira, P.; Maher, R. C.; Garcia-Tunon, E.; Eslava, S.; Agnoli, S.; Mattevi, C.; Saiz, E., Mesoscale assembly of chemically modified graphene into complex cellular networks. *Nat. Commun.* **2014**, *5*, 4328.
29. Zhang, C.; Ma, B.; Zhou, Y., Three-dimensional polypyrrole derived N-doped carbon nanotube aerogel as a high-performance metal-free catalyst for oxygen reduction reaction. *ChemCatChem* **2019**, *11*, 5495-5504.
30. Nguyen, N.; Zhang, S.; Oluwalowo, A.; Park, J. G.; Yao, K.; Liang, R., High-performance and lightweight thermal management devices by 3D printing and assembly of continuous carbon nanotube sheets. *ACS Appl. Mater. Inter.* **2018**, *10*, 27171-27177.
31. Chen, X.; Liu, H.; Zheng, Y.; Zhai, Y.; Liu, X.; Liu, C.; Mi, L.; Guo, Z.; Shen, C., Highly compressible and robust polyimide/carbon nanotube composite aerogel for high-performance wearable pressure sensor. *ACS Appl. Mater. Inter.* **2019**, *11*, 42594-42606.
32. Mujahid, M.; Khan, R. U.; Mumtaz, M.; Soomro, S. A.; Ullah, S., $NiFe_2O_4$ nanoparticles/MWCNTs nanohybrid as anode material for lithium-ion battery. *Ceram. Int.* **2019**, *45*, 8486-8493.
33. Zeng, Y.; Li, T.; Yao, Y.; Li, T.; Hu, L.; Marconnet, A., Thermally conductive reduced graphene oxide thin films for extreme temperature sensors. *Adv. Funct. Mater.* **2019**, *29*, 1901388.
34. Li, T.; Pickel, A. D.; Yao, Y.; Chen, Y.; Zeng, Y.; Lacey, S. D.; Li, Y.; Wang, Y.; Dai, J.; Wang, Y., Thermoelectric properties and performance of flexible reduced graphene oxide films up to 3,000 K. *Nat. Energy* **2018**, *3*, 148-156.
35. Liu, M.; Wang, H.; Wu, S.; Wang, Y.; Qiu, S.; Zhang, S.; Bao, C., Preparation of castable phase change materials beads based on millimeter-sized nanocarbon aerogels for thermal energy storage. *Appl. Therm. Eng.* **2020**, *174*, 115319.
36. Zhang, Q.; Yu, Y.; Yang, K.; Zhang, B.; Zhao, K.; Xiong, G.; Zhang, X., Mechanically robust and electrically conductive graphene-paper/glass-fibers/epoxy composites for stimuli-responsive sensors and Joule heating deicers. *Carbon* **2017**, *124*, 296-307.
37. Yang, Y.; Dong, R.; Zhu, Y.; Li, H.; Zhang, H.; Fan, X.; Chang, H., High-performance direct hydrogen peroxide fuel cells (DHPFCs) with silver nanowire-graphene hybrid aerogel as highly-conductive mesoporous electrodes. *Chem. Eng. J.* **2020**, *381*, 122749.
38. Gao, T.; Li, Y.; Chen, C.; Yang, Z.; Kuang, Y.; Jia, C.; Song, J.; Hitz, E. M.; Liu, B.; Huang, H., Architecting a floatable, durable, and scalable steam generator: hydrophobic/hydrophilic bifunctional structure for solar evaporation enhancement. *Small Methods* **2019**, *3*, 1800176.
39. Kashyap, V.; Al-Bayati, A.; Sajadi, S. M.; Irajizad, P.; Wang, S. H.; Ghasemi, H., A flexible anti-clogging graphite film for scalable solar desalination by heat localization. *J. Mater. Chem. A* **2017**, *5*, 15227-15234.
40. Tao, F.; Zhang, Y.; Wang, B.; Zhang, F.; Chang, X.; Fan, R.; Dong, L.; Yin, Y., Graphite powder/semipermeable collodion membrane composite for water evaporation. S*ol. Energ. Mater. Sol. C.* **2018**, *180*, 34-45.
41. Yang, J.; Pang, Y.; Huang, W.; Shaw, S. K.; Schiffbauer, J.; Pillers, M. A.; Mu, X.; Luo, S.; Zhang, T.; Huang, Y., Functionalized graphene enables highly efficient solar thermal steam generation. *ACS Nano* **2017**, *11*, 5510-5518.

42. Bai, B.; Yang, X.; Tian, R.; Ren, W.; Suo, R.; Wang, H., High-efficiency solar steam generation based on blue brick-graphene inverted cone evaporator. *Appl. Therm. Eng.* **2019**, *163*, 114379.
43. Luo, X.; Huang, C.; Liu, S.; Zhong, J., High performance of carbon-particle/bulk-wood bi-layer system for solar steam generation. *Int. J. Energ. Res.* **2018**, *42* , 4830-4839.
44. Su, H.; Zhou, J.; Miao, L.; Shi, J.; Gu, Y.; Wang, P.; Tian, Y.; Mu, X.; Wei, A.; Huang, L., A hybrid hydrogel with protonated g-C_3N_4 and graphene oxide as an efficient absorber for solar steam evaporation. *Sustain. Mater. Technol.* **2019**, *20*, e00095.
45. Cheng, G.; Wang, X.; Liu, X.; He, Y.; Balakin, B. V., Enhanced interfacial solar steam generation with composite reduced graphene oxide membrane. *Sol. Energy* **2019**, *194*, 415-430.
46. Feng, X.; Zhao, J.; Sun, D.; Shanmugam, L.; Kim, J. K.; Yang, J., Novel onion-like graphene aerogel beads for efficient solar vapor generation under non-concentrated illumination. *J. Mater. Chem. A* **2019**, *7*, 4400-4407.
47. Deng, X.; Nie, Q.; Wu, Y.; Fang, H.; Zhang, P.; Xie, Y., Nitrogen-doped unusually superwetting, thermally insulating and elastic graphene aerogel for efficient solar steam generation. *ACS Appl. Mater. Inter.* **2020**, *23*, 26200-26212
48. Huang, L.; Pei, J.; Jiang, H.; Hu, X., Water desalination under one sun using graphene-based material modified PTFE membrane. *Desalination* **2018***, 442,* 1-7.
49. Ming, X.; Guo, A.; Zhang, Q.; Guo, Z.; Yu, F.; Hou, B.; Wang, Y.; Homewood, K.P.; Wang, X., 3D macroscopic graphene oxide/MXene architectures for multifunctional water purification. *Carbon* **2020**, *167*, 285-295
50. Chen, W.; Zou, C.; Li, X.; Liang, H., Application of recoverable carbon nanotube nanofluids in solar desalination system: an experimental investigation. *Desalination* **2019**, *451*, 92-101.
51. Xiong, Z. C.; Zhu, Y. J.; Qin, D. D.; Chen, F. F.; Yang, R. L., Flexible fire-resistant photothermal paper comprising ultralong hydroxyapatite nanowires and carbon nanotubes for solar energy-driven water purification. *Small* **2018**, *14*, 1803387.
52. Gan, Q.; Zhang, T.; Chen, R.; Wang, X.; Ye, M., Simple, low-dose, durable, and carbon-nanotube-based floating solar still for efficient desalination and purification. *ACS Sustain. Chem. Eng.* **2019**, *7*, 3925-3932.
53. Wang, X.; He, Y.; Liu, X.; Zhu, J., Enhanced direct steam generation via a bio-inspired solar heating method using carbon nanotube films. *Powder Technol.* **2017**, *321*, 276-285.
54. Shi, L.; Wang, Y.; Zhang, L.; Wang, P., Rational design of a bi-layered reduced graphene oxide film on polystyrene foam for solar-driven interfacial water evaporation. *J. Mater. Chem. A* **2017**, *5*, 16212-16219.
55. Liu, S.; Huang, C.; Luo, X.; Rao, Z., High-performance solar steam generation of a paper-based carbon particle system. *Appl. Therm. Eng.* **2018**, *142*, 566-572.
56. Wang, Y.; Wang, C.; Song, X.; Megarajan, S. K.; Jiang, H., A facile nanocomposite strategy to fabricate a rGO-MWCNT photothermal layer for efficient water evaporation. *J. Mater. Chem. A* **2018**, *6*, 963-971.
57. Hu, R.; Zhang, J.; Kuang, Y.; Wang, K.; Cai, X.; Fang, Z.; Huang, W.; Chen, G.; Wang, Z., A Janus evaporator with low tortuosity for long-term solar desalination. *J. Mater. Chem. A* **2019**, *7*, 15333-15340.
58. Yin, Z.; Wang, H.; Jian, M.; Li, Y.; Xia, K.; Zhang, M.; Wang, C.; Wang, Q.; Ma, M.; Zheng, Q. S., Extremely black vertically aligned carbon nanotube arrays for solar steam generation. *ACS Appl. Mater. Inter.* **2017**, *9*, 28596-28603.

Table of Contents Graphic